KSME

Springer

Journal of Mechanical Science and Technology 37 (10) 2023

Original Article
DOI 10.1007/s12206-023-0906-7

Keywords:
· Aero-engine
· High-pressure rotor
· Nonconcentricity
· Bolted structure
· Endface deviation

Correspondence to:
Guo Chen
cgnuaacca@163.com

Citation:
Shen, X., Chen, G. (2023). Study on the nonconcentricity of the high-pressure rotor of the aero-engine. Journal of Mechanical Science and Technology 37 (10) (2023) 4989~5002.
http://doi.org/10.1007/s12206-023-0906-7

Received March 14th, 2023
Revised June 21st, 2023
Accepted June 25th, 2023

† Recommended by Editor
No-cheol Park

Study on the nonconcentricity of the high-pressure rotor of the aero-engine

Xiangxiang Shen[1] and Guo Chen[2]

[1]College of Civil Aviation, Nanjing University of Aeronautics and Astronautics, Nanjing 210016, China, [2]College of General Aviation and Flight, Nanjing University of Aeronautics and Astronautics, Liyang 213300, China

Abstract This paper analyzes the assembly deformation of the aero-engine high-pressure rotor simulation tester, establishes the dynamic model of high-pressure rotor nonconcentricity, simulates the vibration response of the nonconcentric rotor, and verifies the correctness of the dynamic model of rotor nonconcentricity through tests. The results show that the rotor axis line is tapered when there is endface deviation, and the deformation is mainly concentrated in the front end of the tapered drum and the connection surface of the turbine rear journal, and the assembly parameters such as the bolt pretightening force and the number of bolts have little effect on the rotor assembly deformation; in addition, rotor nonconcentricity causes an increase in the rotor vibration amplitude, and the failure characteristics of frequency-doubled appear at the connection structure with endface deviation.

1. Introduction

Aero-engine high-pressure rotors usually contain multiple stop bolt connection structures. Rotor assembly deviations, rotor-stator rubbing, thermal deformation and other factors can cause the rotor connection interface to slip, which will generate deviations between the inertia axis of each rotor component and the rotation axis of rotor, thus resulting in nonconcentricity of a high-pressure rotor [1]. High-pressure rotor nonconcentricity can cause serious accidents such as vibration overload and bearing wear of the whole engine. Therefore, the study of assembly deformation and its vibration response of nonconcentric high-pressure rotor is of great significance for the design of aero-engine high-pressure rotor system connection structure, the rotor system vibration control and the fault diagnosis.

Scholars at home and abroad have proposed nonconcentricity calculation methods and deviation transfer models for single-stage and multi-stage bolted structures of rotor systems, and through the optimized algorithms, have controlled the nonconcentricity during rotor assembling [2-6] and other methods [7]. Meng [8] established the assembly deformation model of the stop bolt connection structure under the conditions of endface deviation and radial deviation, obtained the multi-stage rotor deviation accumulation model, and verified the accuracy of the rotor assembly deformation model through tests. Ye [9] analyzed the assembly deformation mechanism of the stop bolt connection under the condition of endface devia-tion, established the corresponding assembly deformation model, and analyzed the influence law of characteristic parameters such as endface deviation and stop interference magnitude on its deformation degree. Chen [10] established a calculation model of the nonconcentricity of rotor system when the connection structure is randomly misaligned, and analyzed the influence law of structural parameters, process parameters and joint load parameters on the system nonconcentricity. Li [11] used the solid finite element model of bolted flange connection to analyze the influence law of bolt pretightening force on the coaxiality of the structure in detail, and the calculation results showed that the circumferential position of the bolt has some influence on the concentricity of the structure. Through the theoretical calculation model of nonconcentricity, Zhang [12] analyzed the influence law of endface runout and phase on the concentricity of engine case. Bai

[13] established a contact finite element model of multi-bolt connection and analyzed the influence law of pretightening force and tightening sequence on the concentricity of the case.

In terms of the kinetic response to rotor nonconcentricity, rotor nonconcentricity mainly causes rotor shaft line offset, and this failure type is similar to rotor bending. In terms of vibration response and fault characteristics of rotor bending, a lot of research work has been carried out by scholars at home and abroad. Taking a rigidly supported single-disk bended rotor as the research object, Nichola [14] analyzed in detail the influence law of rotor bending excitation and unbalanced excitation on rotor vibration characteristics. On this basis, Shiau [15] further analyzed the vibration characteristics of the Jeffcott rotor during initial bending by considering the effect of disc tilt on the rotor gyroscopic moment during bending in detail. Liu [16] compared and analyzed the vibration characteristics of the Jeffcott rotor, cantilever rotor and double-supported optical shaft rotor under the condition of the initial bending. Lin [17] through taking a rotor with asymmetric stiffness as the research object, analyzed in detail the effect of the angle between the bending direction and the unbalance direction on the dynamic characteristics and vibration stability of the system. After further consideration of rotor cracks, Zou [18] established the dynamic model of rotor crackbending coupling fault, simulated and analyzed the rotor vibration response with and without crack, and researched the stabil-ity of the rotor system by Floquet theory.

In summary, scholars at home and abroad have made abundant research results in nonconcentricity calculation model and nonconcentricity vibration response. However, there are fewer studies on the assembly deformation of nonconcentric high-pressure rotors, and the rotor nonconcentricity model has not yet considered the additional excitation of the connection structure, and the simulation results mostly lack experimental verification. In view of this, a finite element model of a high-pressure rotor simulation tester with multiple bolted connection surfaces is established in this paper to carry out the simulation analysis of rotor assembly deformation under the condition of endface deviation. In addition, a nonconcentricity dynamic model is also established in this paper to analyze the vibration response of rotor nonconcentricity from both simulation and test, thus revealing the fault characteristics and generation mechanism of rotor nonconcentricity.

2. Simulation of assembly deformation of nonconcentric rotors

A typical aero-engine high-pressure rotor is shown in Fig. 1, where there are four stop bolt connection structures at the front and rear, with short bolts pressed axially and the stop cylindrical surface positioned circumferentially. Usually, interference fit is used, but the connection interface often has assembly deviation. This makes the high-pressure rotor inertia axis deflected, therefore leading to rotor nonconcentricity. Since the high-pressure rotor connection structure is usually positioned via stop with small radial deviation, this section establishes a solid

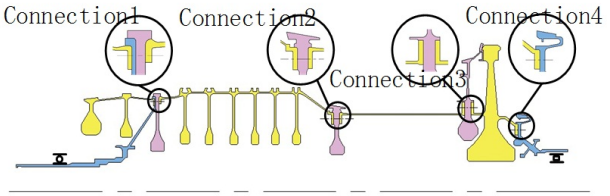

Fig. 1. High-pressure rotor of a typical aircraft engine.

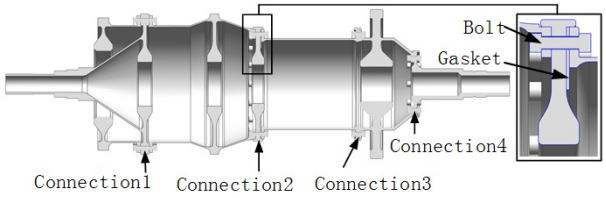

Fig. 2. 3D solid model of high-pressure rotor simulation tester with multiple bolted connection surfaces.

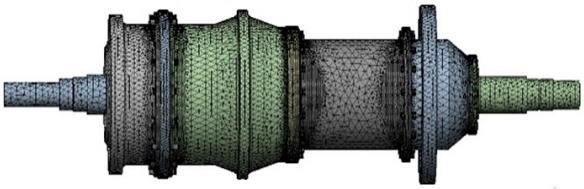

Fig. 3. Finite element model of high-pressure rotor simulation tester with multiple bolted connection surfaces.

finite element model of the high-pressure rotor simulation tester with multiple bolted connection surfaces to analyze in detail the assembly deformation of the high-pressure rotor simulation tester under the condition of endface deviation.

2.1 Solid finite element model

A 3D modeling software UG is used to build the 3D solid model of the high-pressure rotor simulation tester. As shown in the Fig. 2, a gasket is added at the position of connection 2, and the endface deviation of connection 2 is simulated by changing the inclination angle of the gasket. Besides, ANSYS Workbench finite element analysis software is used to build a solid finite element model of the high-pressure rotor simulation tester with multiple bolted connection surfaces. As shown in the Fig. 3, the model is meshed with SOLID187 tetrahedral cells, and meshes are refined locally in four connection parts with M8 bolts. The model is made of 45# steel, whose basic material properties include modulus of elasticity 207000 MPa, Poisson's ratio 0.3, and density 7800 kg/m^3.

The loads and restraints of the solid finite element model of the tester are shown in the Fig. 4, where fixed constraints are set at the bearing positions on the left and right sides, and the bolt pretightening force is applied at the four stop bolt connection positions at the front and rear through PRETS179 pretightening force unit. The bolt pretightening force is set to 10313 N

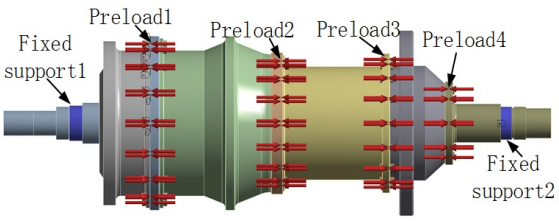

Fig. 4. High-pressure rotor simulation tester load and restraint settings.

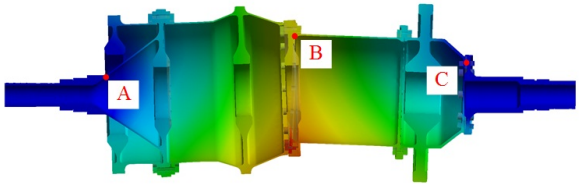

Fig. 5. Section of the assembly deformation of the high-pressure rotor simulation tester.

according to the HB6125 standard. 22 sets of contact surfaces are provided at the front and rear, which adopt CONTA174 and TARGE170 units to create contact pairs. A friction contact type with a friction coefficient of 0.15 is used. The offset option of the contact surface at the stop position is set to 0.04 mm to simulate the interference fit in the stop area. Eventually, the deformation of the whole rotor is calculated by extracting the displacement of the nodes on the axis line.

2.2 Finite element analysis of assembly deformation

The assembly deformation of the high-pressure rotor simulation tester when the endface deviation is 1mm is shown in the Fig. 5. The radial displacement of the axis line node is extracted and the axis line deformation is plotted according to the axial position of the node, as shown in the Fig. 6. The overall high-pressure rotor simulation tester is tapered, and the radial deviation at point B where the gasket is added is the largest, with a maximum radial deviation of 0.6383 mm. From the axis line deformation diagram, we can see that the rotor bends at points A and C. Point A is located at the front of the conical drum of the high-pressure rotor, where the rigidity is weak, while point C is located at the connection surface 4 of the stop bolt. Due to the small number of bolts and the weak connection stiffness, the bolted connection surface is separated, and the axis lines before and after points A and C are straight, indicating that the overall stiffness of all parts of the high-pressure rotor is high and no bending deformation occurs.

The contact state of each connection surface before and after the rotor is shown in the Fig. 6. The simulation results show that under the action of the bolt pretightening force, the endface deviation application position (i.e. bolted connection surface 2) achieves a good fit, the bolted connection surface 1 and bolted connection surface 3 have a good contact state, and the bolted connection surface 4 is separated, which corresponds to the change of radial deviation at point C.

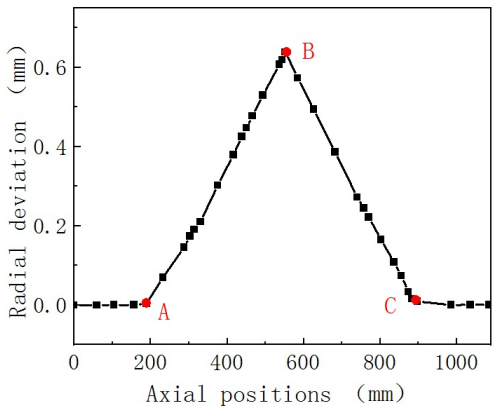

Fig. 6. Deformation of the rotor axis line of the high-pressure rotor simulation tester.

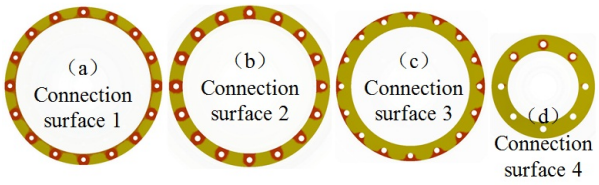

Fig. 7. Contact state of the bolted connection surface.

2.3 Influence law of characteristic parameters

The characteristic parameters such as endface deviation, bolt pretightening force and number of bolts may have some influence on the assembly deformation of the high-pressure rotor simulation tester. This subsection discusses in detail the influence law of these three characteristic parameters on rotor assembly deformation.

2.3.1 Endface deviation

The deformation of the rotor axis line with different endface deviations is shown in the Fig. 8. As can be seen from the figure, with the increasing endface deviation, the radial deviation of the high-pressure rotor simulation tester is increasing, and the deformation of the axis line is becoming more and more obvious, and the nonconcentricity of the rotor is increasing. Under the conditions of 0.5 mm, 1.0 mm, 1.5 mm and 2.0 mm endface deviations, the maximum values of rotor radial runout are 0.3177 mm, 0.6383 mm, 0.9135 mm and 1.2181 mm, respectively, and the maximum radial runout value of rotor is basically linear with the endface deviation. This indicates that the connection surface 2 maintains a good fit at different endface deviations, and the main deformation parts are still mostly located in the front end of the conical drum cylinder and the bolted connection surface 4.

2.3.2 Bolt pre-tightening force

The deformation of the rotor axis line under different pre-

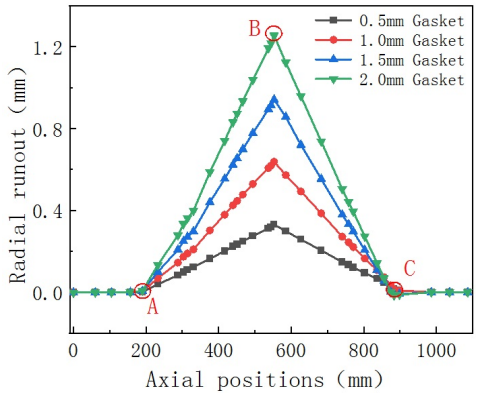

Fig. 8. Deformation of rotor axis line at different gasket inclination angles.

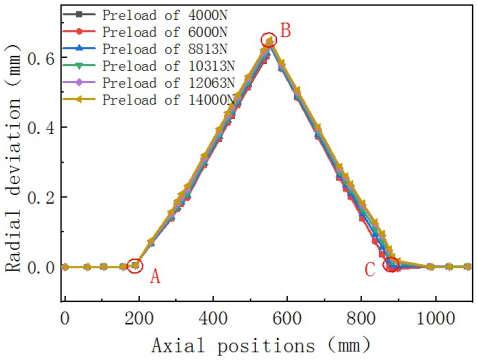

Fig. 9. Deformation of the axis line of the high-pressure rotor simulation tester under different pretightening forces.

tightening forces is shown in the Fig. 9. When the endface deviation is certain, the radial deviation of the rotor remains basically the same with the increase of pretightening force. This indicates that the connection surface 1, connection surface 2 and connection surface 3 all maintain a good fit under different pretightening forces. The radial deviation at the connection surface 4 (point C) increases slightly as the pretightening force decreases, because the bolt connection 4 undergoes significant separation and deformation when the pretightening force is small, causing the right rotor to warp upward. Overall, the bolt pretightening force has a small effect on rotor assembly deformation.

2.3.3 Number of bolts

The deformation of rotor axis line at different number of bolts is shown in the Fig. 10. As the number of bolts decreases, the radial deflection of the rotor keeps decreasing. The radial displacement of point B is 0.6383 mm, 0.5705 mm and 0.5062 mm for 16, 8 and 4 bolts respectively, which indicates that the contact condition of connection surface 2 deteriorates as the number of bolts decreases, and the connection surface cannot fit completely, resulting in a decrease in the radial deflection of the rotor axis line. At the same time, as the number of bolts decreases, the rotor axis line inflects at point D, the position of which corresponds to connection surface 1. This indicates that

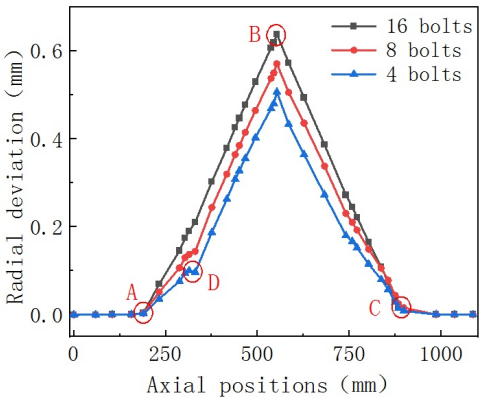

Fig. 10. Deformation of the axis line of the high-pressure rotor simulation tester under different bolt Qty.

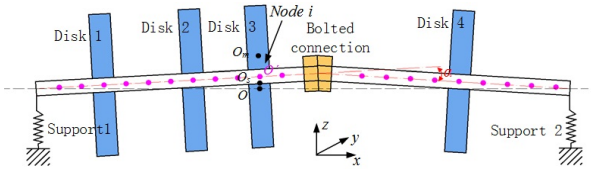

Fig. 11. Nonconcentricity of rotor.

as the number of bolts decreases, the connection surface 1 also gradually separates.

3. Mechanical modeling of nonconcentric rotors and verification

3.1 Mechanical modeling of nonconcentric rotors

From the above, it can be seen that the connection 2 has the most significant influence on the dynamic characteristics of the rotor system and the rotor axis line as a whole is tapered when there is endface deviation at the connection surface. The nonconcentric rotor assembled is shown in the Fig. 11. There is a deviation between the geometric center line of left drum cylinder and right drum cylinder and the rotation center line, which leads to the existence of unbalanced excitation force and bending excitation force that rotates synchronously with the rotor during the rotor rotation. At the same time, there is an angular deviation α from the axis line of the drums on the left and right sides of the stop bolt connection structure, resulting in additional excitation forces in the connection structure similar to the angular misalignment of the coupling. In view of the above two types of additional loads, a rotor dynamic model considering nonconcentricity is developed. Its differential equation of motion can be expressed as:

$$\begin{cases} \mathbf{M}_1\ddot{\mathbf{q}}_1 + (\mathbf{C}_1 - \omega\mathbf{G}_1)\ \dot{\mathbf{q}}_1 + \mathbf{K}_1\mathbf{q}_1 = \\ \mathbf{Q}_{b1} + \mathbf{Q}_{s1} + \mathbf{Q}_{m1} \\ \mathbf{M}_2\ddot{\mathbf{q}}_2 + (\mathbf{C}_2 - \omega\mathbf{G}_2)\dot{\mathbf{q}}_2 + \mathbf{K}_2\mathbf{q}_2 = \\ \mathbf{Q}_{b2} + \mathbf{Q}_{s2} + \mathbf{Q}_{m2}. \end{cases} \quad (1)$$

Where: $\ddot{\boldsymbol{q}}_1$, $\dot{\boldsymbol{q}}_1$ and $\boldsymbol{q}_1$ are the node acceleration, velocity and displacement of the left drum, respectively. $\ddot{\boldsymbol{q}}_2$, $\dot{\boldsymbol{q}}_2$ and $\boldsymbol{q}_2$ are the node acceleration, velocity and displacement of the right drum, respectively. $\boldsymbol{\omega}$ is the rotor angular velocity. $\boldsymbol{M_1}$ and $\boldsymbol{M_2}$ are the mass matrices of the left and right drums. $\boldsymbol{k_1}$ and $\boldsymbol{K_2}$ are the stiffness matrices of the left and right drums. $\boldsymbol{G_1}$ and $\boldsymbol{G_2}$ are the gyroscopic matrices of the left and right drums. $\boldsymbol{C_1}$ and $\boldsymbol{C_2}$ are the damping matrices of the left and right drums. The system damping is proportional damping, i.e. $\boldsymbol{C} = \alpha\boldsymbol{M}+\beta\boldsymbol{K}$. $\boldsymbol{M}$ is the corresponding system mass matrix, $\boldsymbol{K}$ is the corresponding system stiffness matrix, α is the mass damping coefficient, β is the stiffness damping coefficient. $\boldsymbol{Q}_{b1}$ and $\boldsymbol{Q}_{b2}$ are the additional excitation forces resulting from the relative motion of the rotors at the left and right ends of the coupling. $\boldsymbol{Q}_{s1}$ and $\boldsymbol{Q}_{s2}$ are the additional excitation forces caused by the nonconcentricity of the left and right drums, including both unbalanced and bending excitation forces. $\boldsymbol{Q}_{m1}$ and $\boldsymbol{Q}_{m2}$ are the additional excitation forces of the connection structure caused by the nonconcentricity.

When the assembled rotor is nonconcentric, the initial radial bend of the left drum is $\boldsymbol{b_1}$ and the offset of the center of mass of the turntable is $\boldsymbol{\delta_1}$. Take node *i* as an example. When it has radial bending and mass eccentricity, the position of the disc where node *i* is located is shown in the Fig. 12, where *O* is the center of rotation, O_s is the geometric center after the deviation of the center of rotation *O* due to the initial bending, *O´* is the geometric center of the disc vortex state, O_m is the center of mass of the disc, and the vector OO_s is the radial offset of node i, whose projections in the y-direction and z-direction are b_{yi} and b_{zi}, respectively. Therefore, when the initial bending exists at node *i*, the initial bending quantity $\boldsymbol{b_1}$ can be expressed as:

$$\mathbf{b}_1 = \left\{ 0 \quad \cdots \quad \overbrace{0 \quad b_{yi} \quad b_{zi} \quad 0 \quad 0 \quad 0}^{\text{freedom of ith node}} \quad \cdots 0 \right\}^{\mathrm{T}} . \tag{2}$$

The vector $O'O_m$ is the mass eccentricity of node i, whose projections in the y-direction and z-direction are δ_{yi} and δ_{zi}, respectively. Therefore, when mass eccentricity exists at node *i*, the initial eccentricity δ_1 can be expressed as:

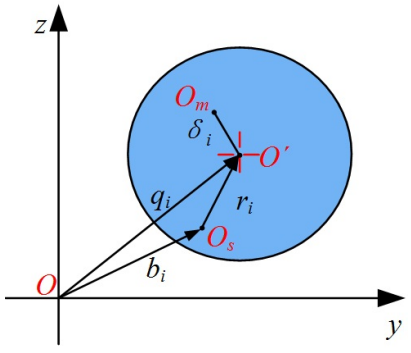

Fig. 12. Position of turntable.

$$\boldsymbol{\delta}_1 = \left\{ 0 \quad \cdots \quad \overbrace{0 \quad \delta_{yi} \quad \delta_{zi} \quad 0 \quad 0 \quad 0}^{\text{freedom of ith node}} \quad \cdots 0 \right\}^{\mathrm{T}} . \tag{3}$$

The load induced by the initial bend amount $\boldsymbol{b_1}$ of the rotor is the excitation force $\boldsymbol{K_1 b_1}$ that rotates synchronously with the rotor. The additional unbalanced excitation force induced by the eccentricity $\boldsymbol{\delta_1}$ of the wheel disc mass is $\boldsymbol{M_1 \delta_1 \omega^2}$. So, the additional excitation force $\boldsymbol{Q}_{s1}$ induced by the nonconcentricity of the left drum can be expressed as:

$$\mathbf{Q}_{s1} = \mathbf{K}_1\mathbf{b}_1 + \mathbf{M}_1\boldsymbol{\delta}_1\omega^2 . \tag{4}$$

Similarly, the additional excitation force $\boldsymbol{Q}_{s2}$caused by the nonconcentricity of the right drum can be obtained as:

$$\mathbf{Q}_{s2} = \mathbf{K}_2\mathbf{b}_2 + \mathbf{M}_2\boldsymbol{\delta}_2\omega^2 . \tag{5}$$

Where $\boldsymbol{b_2}$ is the initial bend amount of the right drum, and $\boldsymbol{\delta_2}$ is the offset of the center of mass of the right drum turntable.

The left drum and the right drum are connected by a stop bolt connection structure that is simulated by adding additional excitation forces $\boldsymbol{Q}_{b1}$ and $\boldsymbol{Q}_{b2}$ generated by the relative motion of the rotor at the left and right ends of the coupling. Assuming that node i of the left drum is connected to node j of the right drum, and the radial force and bending moment are transferred between them through the stop bolt connection structure, the radial force and bending moment of node i can be expressed as:

$$\begin{cases} F_{yi}^1 = k_{ny}(y_j^2 - y_i^1) + c_{ny}(\dot{y}_j^2 - \dot{y}_i^1) \\ F_{zi}^1 = k_{nz}(z_j^2 - z_i^1) + c_{nz}(\dot{z}_j^2 - \dot{z}_i^1) \\ M_{yi}^1 = k_{\theta y}(\theta_{jy}^2 - \theta_{iy}^1) + c_{\theta y}(\dot{\theta}_{jy}^2 - \dot{\theta}_{iy}^1) \\ M_{zi}^1 = k_{\theta z}(\theta_{jz}^2 - \theta_{iz}^1) + c_{\theta z}(\dot{\theta}_{jz}^2 - \dot{\theta}_{iz}^1) \end{cases} . \tag{6}$$

Where F_{yi}^1 and F_{zi}^1 denote the forces on the left drum node i in the y-direction and z-direction, respectively. M_{yi}^1 and M_{zi}^1 are the moments of the left drum node i around the y-axis and the z-axis. k_{ny} and k_{nz} are the radial stiffnesses of the connection structure in the y-direction and z-direction. $k_{\theta y}$ and $k_{\theta z}$ are the bending stiffnesses of the connection structure around the y-axis and the z-axis. c_{ny} and c_{nz} denote the radial damping of the connection structure. $c_{\theta y}$ and $c_{\theta z}$ represent the angular damping of the connected structure. According to the principle of mutuality of forces, the forces F_{yj}^2 and F_{zj}^2 and the moments M_{yj}^2 and M_{zj}^2 on the right drum node j are the reaction forces and reaction moments of node i.

The additional excitation force for the endface deviation of the bolted connection surface is set by Ref. [19]. For the angular deviation of the left and right rotor axis lines caused by the endface deviation of the bolted connection surface, the simplified model mainly considers the following three uncertainty factors:

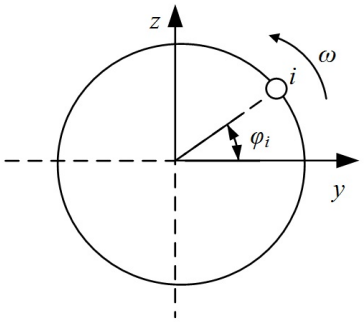

Fig. 13. Circumferential position of the connected pair.

① Uneven circumferential position of the bolt

As shown in the Fig. 13, the circumferential position of bolt i at t can be expressed as:

$$\phi_i(t)=\frac{(i-1)\times 2\pi}{N}+\phi_0+\omega t+r_i\times(\frac{\Delta_{\mathrm{Deg}}\pi}{180})\quad(i=1,2,\cdots,N)\ . \tag{7}$$

Where N is the number of connected pairs, ϕ_0 is the circumferential position in the initial angular misalignment, Δ_{Deg} is the discrete angle of the circumferential position, and r_i is a random number from -1 to 1. The discrete angle Δ_{Deg} and the random number r_i are used to model the inhomogeneity of the circumferential position distribution.

② Different axial stiffness of the bolt

Due to assembly and manufacturing errors, there is some variation in the connection stiffness of each bolt in the circumferential direction. Therefore, the stiffness dispersion coefficient ξ is introduced to characterize the variability of the axial stiffness of the bolts, i.e., the axial stiffness of the *i*-th bolt connection is expressed as:

$$k_{ai}=(1+\xi\times r_i)\times k_{\mathrm{a}}\ . \tag{8}$$

Where k_a is the average axial stiffness of the bolt, and r_i is a random number from -1 to 1.

③ Non-linear characteristics of the bolt stiffness

The axial stiffness of the bolt is similar to that of a rigid spring to some extent. Therefore, the nonlinear stiffness characteristics of the bolt similar to those of the rigid spring are simulated, and the nonlinear axial force of the i^{th} bolt is expressed as:

$$F_{xi}=k_{\mathrm{a}}\delta_{ai}+\varepsilon\delta_{ai}^{3}\ . \tag{9}$$

Where δ_{ai} is the axial relative displacement of the nodes on both sides of the bolt, and ε is the nonlinear factor.

Considering the above three nonlinear factors, the additional excitation force triggered by the angular deviation of the bolted connection surface is deduced. At *t*, the angular deviation of the connection surface is $\boldsymbol{\theta}$, the radius of action of the bolt is R_b, and the axial deformation δ_{ai} of the i^{th} bolt can be expressed as:

$$\delta_{ai}(t)=-R_{\mathrm{b}}\sin\theta\cos\phi_i(t) \tag{10}$$

The axial force of the i^{th} bolt can be obtained by bringing it into Eq. (9):

$$F_{xi}(t)=k_{ai}\delta_{ai}(t)+\varepsilon\delta_{ai}^{\ 3}(t)\ . \tag{11}$$

The moments of the i^{th} bolt around the y-axis and z-axis are:

$$\begin{cases}M_{yi}(t)=F_{xi}(t)R_{\mathrm{b}}\sin\phi_i(t)\\ M_{zi}(t)=-F_{xi}(t)R_{\mathrm{b}}\cos\phi_i(t).\end{cases} \tag{12}$$

Therefore, the additional excitation force on the left bolted connection surface at *t* is:

$$\begin{cases}F_x^{\mathrm{m}}=\sum_{i=1}^{N}F_{xi}(t)\\ M_y^{\mathrm{m}}=\sum_{i=1}^{N}M_{yi}(t)\\ M_z^{\mathrm{m}}=\sum_{i=1}^{N}M_{zi}(t).\end{cases} \tag{13}$$

Obviously, the additional excitation force acting on the right bolted connection surface is the counter force of Eq. (13).

Since the bolt connection structure is connected to the left rotor node *i* and the right rotor node *j*, the additional excitation forces $\boldsymbol{Q}_{m1}$ and $\boldsymbol{Q}_{m2}$ generated by the angular deviation of the connection interface between the left drum and the right drum can be expressed as:

$$\mathbf{Q}_{m1}=\left\{0\ \cdots\ \overbrace{F_x^{\mathrm{m}}\ \ 0\ \ 0\ \ 0\ \ M_y^{\mathrm{m}}\ \ M_z^{\mathrm{m}}}^{\text{freedom of ith node}}\cdots\ 0\right\}^{\mathrm{T}} \tag{14}$$

$$\mathbf{Q}_{m2}=\left\{0\ \cdots\overbrace{-F_x^{\mathrm{m}}\ \ 0\ \ 0\ \ 0\ \ -M_y^{\mathrm{m}}\ \ -M_z^{\mathrm{m}}}^{\text{freedom of jth node}}\ \cdots\ 0\right\}^{\mathrm{T}}\ . \tag{15}$$

3.2 Comparative verification of modal test and modal simulation

In order to verify the correctness of the dynamic model of the high-pressure rotor with different heart faults, the modal test based on the tester and the modal simulation calculation based on the dynamic equation were carried out.

1) Modal test

The modal test site is shown in Fig. 14. The modal test adopts the sine wave excitation method. The frequency range is 20-300 Hz, and the frequency sweep interval is 1 Hz. The single-input and multi-output modal parameter identification method is adopted. The sinusoidal excitation force is applied to the middle drum position of the rotor, and the excitation force amplitude is 40 N. Seven measuring points are selected on the rotor tester to collect the acceleration signal. The measuring point arrangement scheme is shown in Fig. 15.

After processing the test data, the amplitude-frequency

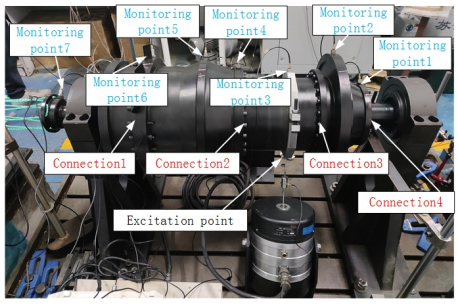

Fig. 14. Modal test site.

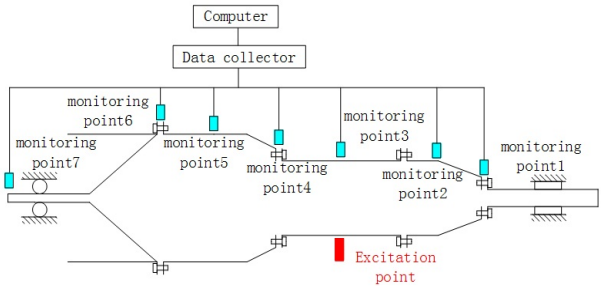

Fig. 15. Signal acquisition point layout scheme diagram.

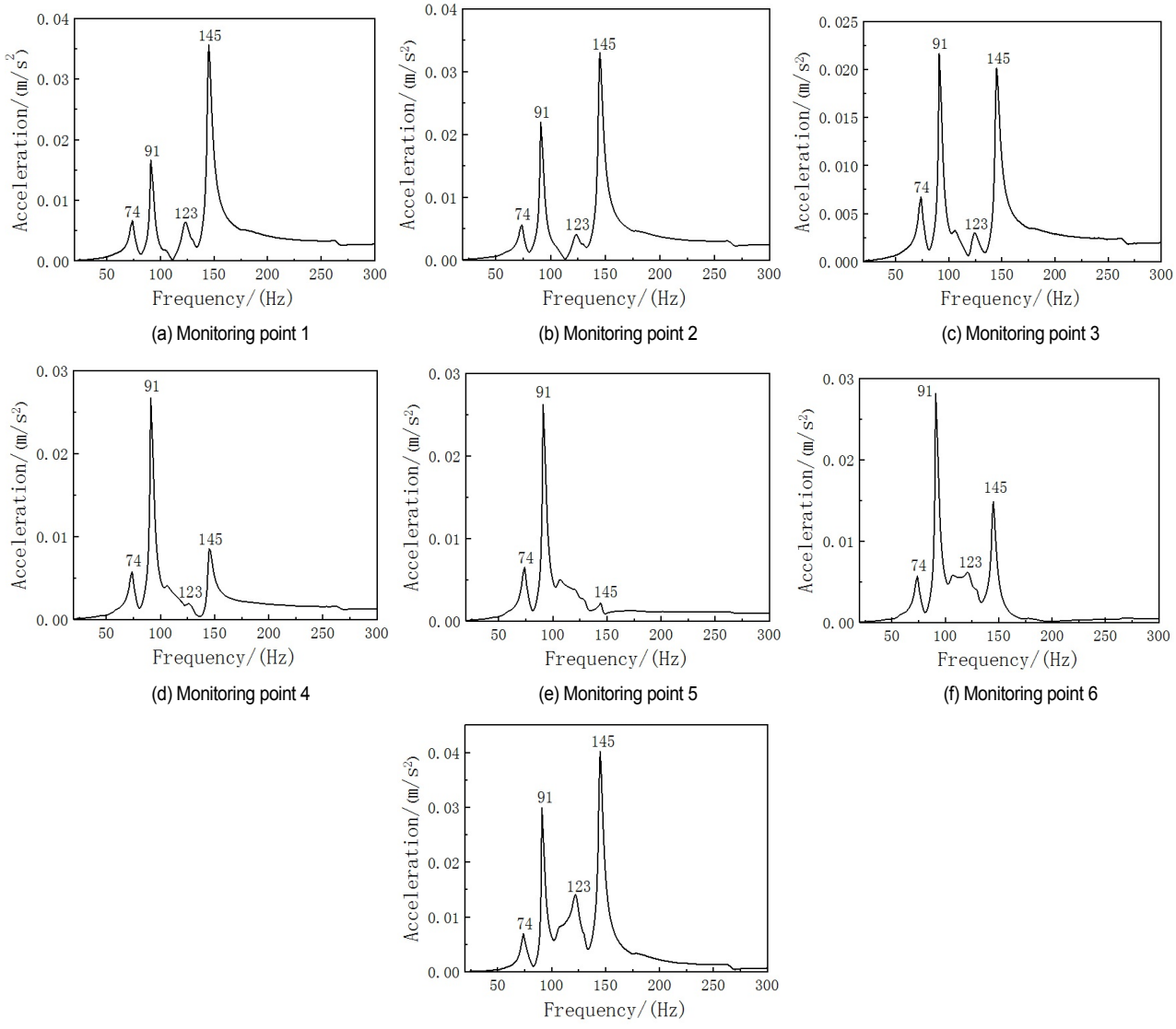

(a) Monitoring point 1

(b) Monitoring point 2

(c) Monitoring point 3

(d) Monitoring point 4

(e) Monitoring point 5

(f) Monitoring point 6

(g) Monitoring point 7

Fig. 16. The amplitude-frequency curve of each measuring point in modal test.

curves of each acceleration measuring point are obtained as shown in Fig. 16. The test results show that there are 4-order resonance frequencies in the sweep frequency range of 20 ~ 300 Hz, which are 74 Hz, 91 Hz, 123 Hz and 145 Hz respectively. The first two resonance frequencies are the first-order natural frequencies of the rotor, and the last two resonance frequencies are the second-order natural frequencies of the rotor. The reason for the two resonance frequencies in each

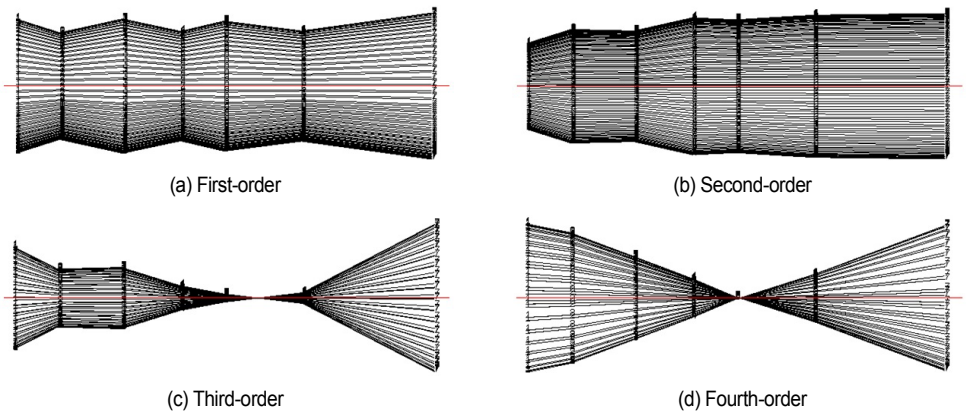

(a) First-order (b) Second-order

(c) Third-order (d) Fourth-order

Fig. 17. Vibration mode of modal test.

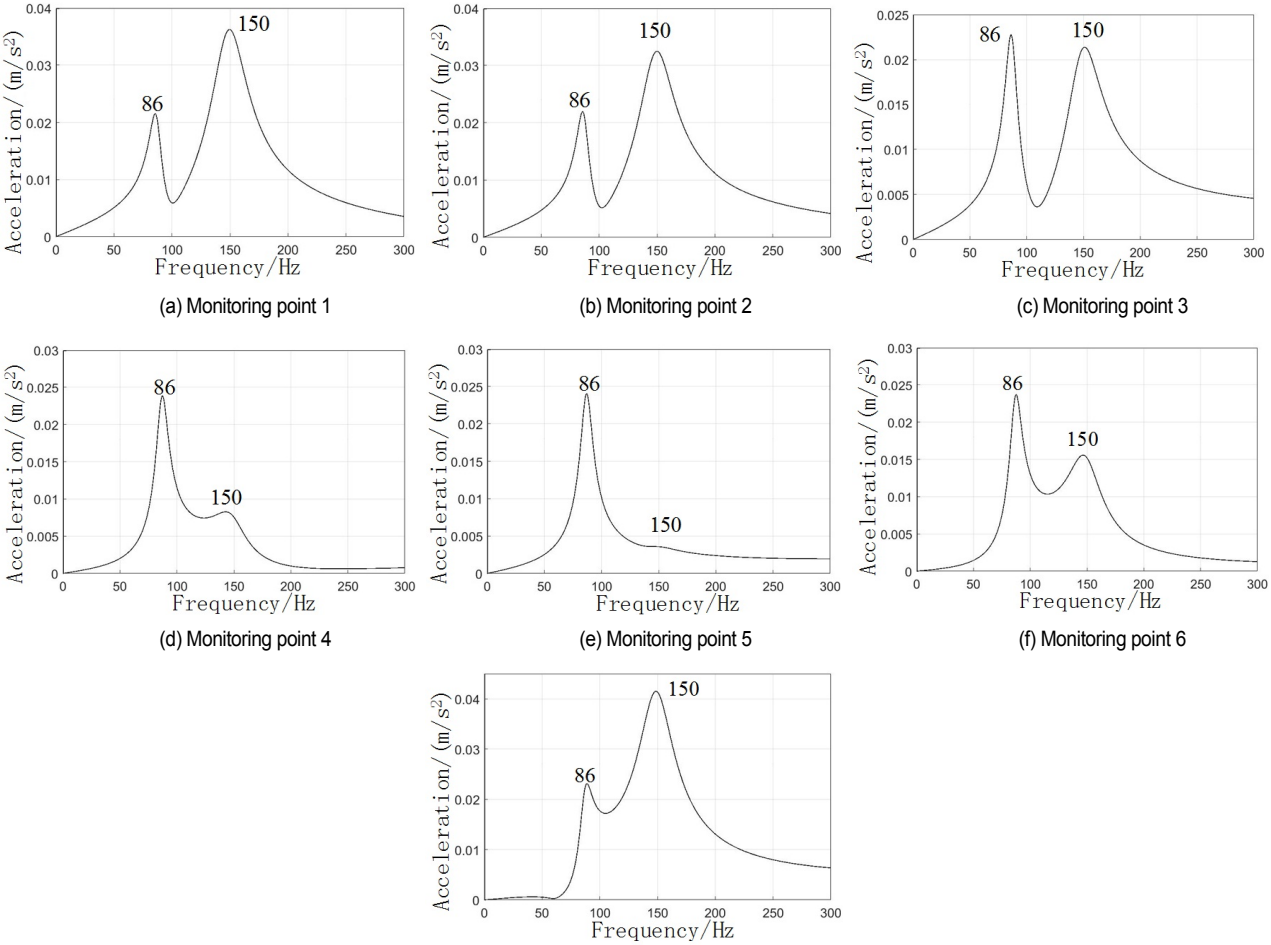

(a) Monitoring point 1 (b) Monitoring point 2 (c) Monitoring point 3

(d) Monitoring point 4 (e) Monitoring point 5 (f) Monitoring point 6

(g) Monitoring point 7

Fig. 18. The amplitude-frequency curve of each measuring point in modal simulation.

mode is that the horizontal and vertical stiffness of the rotor are different. The modal shape of the tester is shown in Fig. 17. The first and second modes are the rotor translation, and the third and fourth modes are the rotor pitch, which further verifies that the first two order resonance frequencies of the rotor are the first order modal frequencies of the tester, and the last two order resonance frequencies are the second order modal frequencies of the tester. In this paper, 91 Hz and 145 Hz are selected as the first two natural frequencies of the rotor, and the first two vibration modes of the rotor are rotor translation and rotor pitch.

2) Modal simulation

Table 1. Natural frequency simulation and experimental comparison.

Order	Natural frequency/(Hz)		Error/(%)
	Test	Simulation	
First	91	86	5.49
Second	145	150	3.45

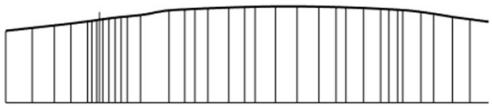

(a) First-order

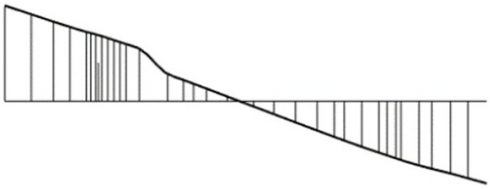

(b) Second-order

Fig. 19. The vibration mode of modal simulation.

According to the high-pressure rotor dynamics model established in this paper, the state space method is used to solve the first two natural frequencies and vibration modes of the rotor system, and the vibration signal of the acceleration measuring point position of the rotor modal test is extracted. The amplitude-frequency curve of each measuring point is shown in Fig. 18. The simulation results show that in the frequency range of 0~300 Hz, the rotor tester has a total of 86 Hz and 150 Hz two-order natural frequencies. The natural frequency simulation and calculation results are shown in Table 1, and the two-order natural frequency errors are within 10 %. The calculation results of the modal shape of the tester are shown in Fig. 19. The first-order modal shape is the rotor translation, and the second-order modal shape is the rotor pitch. The modal shape is consistent with the test results, which verifies the correctness of the rotor dynamics model.

4. Simultion analysis and experimental verification of the vibration response of nonconcentric rotors

According tothe modeling method of a six-degree-of-freedom Timoshenko beam cell and the equivalent method of a rigid disk and support system described in the Ref. [20], the dynamic model of a high-pressure rotor simulation tester containing a stop-bolt connection structure is established. Using the above dynamic model of nonconcentricity and the Newmark-β numerical integration method, the vibration response simulation analysis of nonconcentric rotor is carried out. In the numerical simulation, the angle dispersion coefficient is set to 1.5° and the connected pair stiffness dispersion coefficient to 0.15, considering the uneven bolt circumferential position and different bolt axial stiffness.

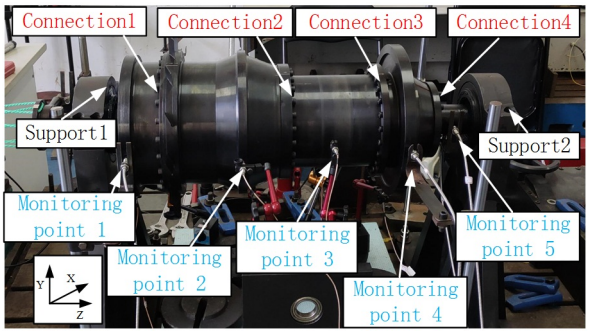

Fig. 20. Test site for rotor nonconcentricity vibration response.

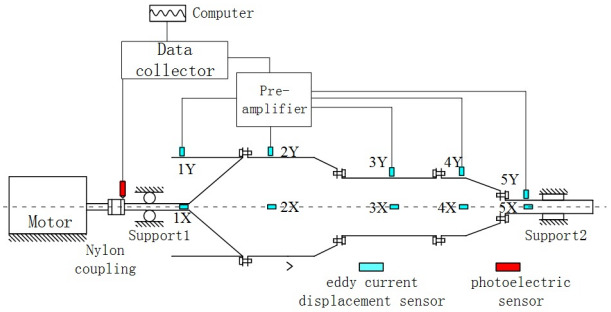

Fig. 21. Signal acquisition measurement point arrangement scheme.

Meanwhile, vibration response simulation tests of nonconcentricity are carried out on the high-pressure rotor simulation tester with multiple bolted connection surfaces, so as to measure the time and frequency domain signals of the system vibration response for nonconcentric rotors and to verify the correctness of the dynamic model for rotor nonconcentricity.

4.1 Introduction of the test device and test system

The high-pressure rotor simulation tester with multiple bolted connection surfaces is shown in the Fig. 20. The tester consists of multiple drum structure segments, there are a total of four stop bolt connection structures at the front and rear, and the left and right ends are fixed by support 1 and support 2 respectively. The connection 2 position is equipped with gaskets. Different degrees of nonconcentricity are simulated by replacing the gaskets with different inclination angles.

The arrangement scheme of the signal acquisition points is shown in the Fig. 21. Eddy current displacement sensors are installed at the right rotation axis of support 1, the drum between connection 4 and connection 3, the drum between connection 3 and connection 2, the drum between connection 2 and connection 1, and the cantilever drum on the right side of connection 1. The obtained vibration displacement signal is amplified by a preamplifier, then collected by a data collector, and finally output to the computer terminal. The nylon rope type coupling is attached with reflective film, and the rotor speed is measured by photoelectric sensor, and the signal is collected

by data collector and then output to the computer side.

The main test steps of the vibration response test of the nonconcentric rotor are: when the tester is not gasketed, the rotor tester is concentric by default, which is regarded as the nonconcentricity condition 1; after the rotor tester is accelerated to 3000 r/min and 4000 r/min in turn, the vibration displacement of measurement points 1~5 at the fixed speed is measured; the gasket with 0.1 mm endface deviation is replaced, which is recorded as the nonconcentricity condition 2; finally, complete the vibration signal measurement at the above characteristic speed and then record the data. In the numerical simulation, the radial deviation of the rotor under different operating conditions is used as input data. Similarly, two characteristic speeds of 3000 r/min and 4000 r/min are selected for the vibration response analysis of nonconcentricity. The experimental results are compared to verify the correctness of the nonconcentricity models.

4.2 Analysis of simulation results and test results

4.2.1 Concentricity

① Spped 3000 r/min

Under concentric state, when the rotor speed is 3000 r/min, the simulation and test results of the vibration response of the front and rear measurement points are shown in the Fig. 22. From the test results, it can be seen that the vibration displacement of measurement point 3 is the largest, with an amplitude of about 0.0373 mm, and the vibration displacement of measurement point 1 is the smallest, with an amplitude of about 0.0136 mm. The vibration signal at each measurement point before and after the rotor is mainly at 1X frequency and shows 2X and 4X frequency characteristics. The simulated signal has only 1X frequency characteristics, which match the frequency spectrum of the test results. Meanwhile, the vibration amplitudes are similar to the test results, which indicates that the initial unbalance of the rotor is effectively set to simulate the initial unbalance state of the rotor tester. In general, the amplitude of vibration displacement at each measurement point before and after the rotor is small, which indicates that the unevenness of the rotor is small and the rotor generally maintains good concentricity.

② Speed 4000 r/min

Under concentric state, when the rotor speed is 4000 r/min, the simulation and test results of the vibration response spectrum plot of all the front and rear measurement points are shown in the Fig. 23. From the spectrum plot of the test results, it can be seen that the rotor still has the maximum vibration displacement at the position of measurement point 3, with the vibration displacement amplitude of about 0.0544 mm, and the vibration response of each measurement point of the rotor is mainly at 1X frequency and shows 2X and 1/2 frequency division characteristics. Compared with the rotor vibration response at 3000 r/min, the vibration displacement amplitude of each measurement point has increased significantly. From the spectrum plot of the simulation results, it can be seen that the

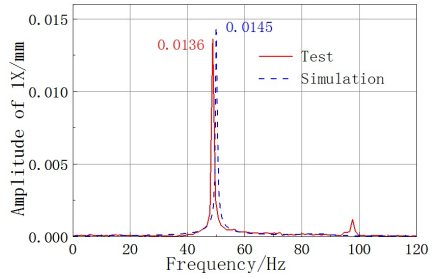

(a) Measurement point 1

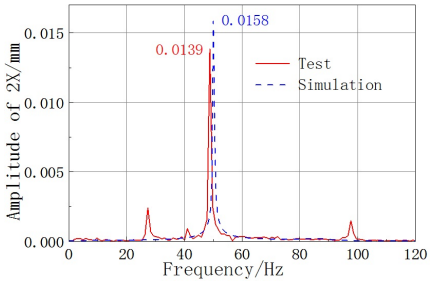

(b) Measurement point 2

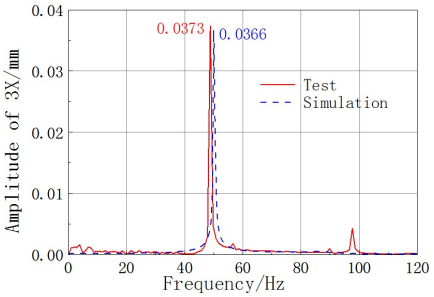

(c) Measurement point 3

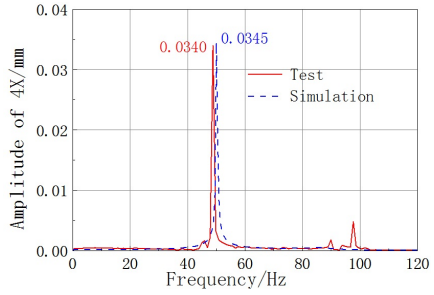

(d) Measurement point 4

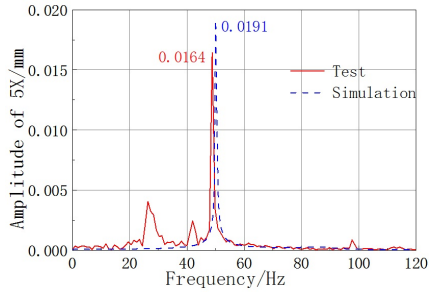

(e) Measurement point 5

Fig. 22. Spectrum plot of the vibration response of each measurement point under concentric state (3000 r/min).

Table 2. Comparison of simulation and experimental results of vibration displacement amplitude at each characteristic speed under concentric state.

Speed	Name	Measurement point 1	Measurement point 2	Measurement point 3	Measurement point 4	Measurement point 5
Characteristic speed 3000 r/min	Test amplitude/mm	0.0136	0.0139	0.0373	0.034	0.0164
	Simulation amplitude/mm	0.0145	0.0158	0.0366	0.0345	0.0191
	Error %	6.62 %	13.67 %	1.88 %	1.47 %	16.46 %
Characteristic speed 4000 r/min	Simulation amplitude/mm	0.0355	0.0324	0.0544	0.0324	0.0322
	Test amplitude/mm	0.0325	0.0359	0.0521	0.0383	0.0338
	Error %	8.45 %	10.80 %	4.23 %	18.21 %	4.97 %

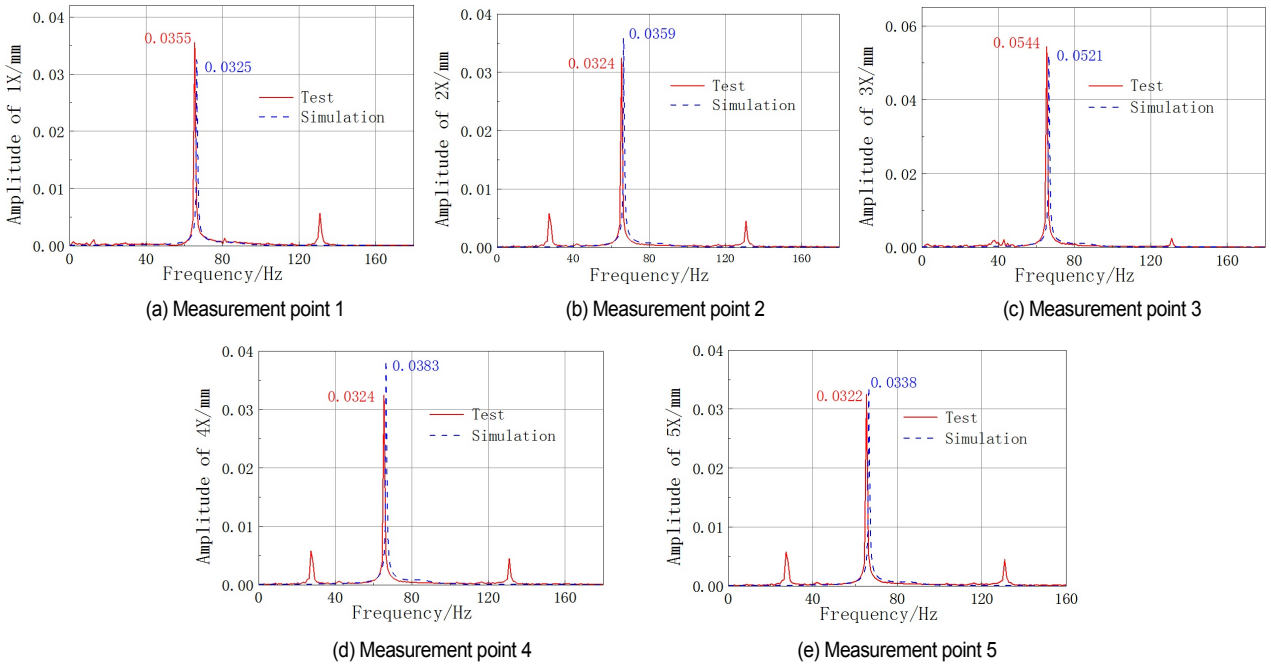

(a) Measurement point 1 (b) Measurement point 2 (c) Measurement point 3

(d) Measurement point 4 (e) Measurement point 5

Fig. 23. Spectrum plot of the vibration response of each measurement point under concentric state (4000 r/min).

vibration response of the simulation results contains only 1X frequency characteristics, and its vibration amplitude is similar to the experimental results, which verifies the correctness of the initial model in this paper.

The comparison between the simulation results and the experimental results of the vibration response amplitude of each measurement point at different characteristic speeds is shown in the Table 2. At different characteristic speeds, the vibration amplitude of each measurement point is similar, and the simulation error does not exceed 20 %, so that the test and simulation are in good agreement. This indicates that the rotor dynamic model established in this paper effectively simulates the initial unbalance state of the rotor tester.

4.2.2 0.1 mm endface deviation

① Speed 3000r/min

Under the condition of 0.1 mm endface deviation, when the rotor speed is 3000 r/min, the test and simulation results of the vibration response spectrum plot of all the front and rear measurement points are shown in the Fig. 24. As shown in the spectrum plot of test results, the vibration response of measurement point 4 is the largest, with the vibration displacement amplitude of about 0.0545 mm; the vibration response of measurement point 5 is the smallest, with the vibration displacement amplitude of about 0.0191 mm; by comparing the rotor vibration response at 3000 r/min under concentric state, it can be seen that the vibration amplitude of each measurement point before and after the rotor has increased, for example, the displacement amplitude of measurement point 4 has increased from 0.0340 mm to 0.0545 mm; at the same time, as shown in the spectrum plot of each measurement point, measurement point 3 and measurement point 4 near the connection 2 show obvious 2X frequency characteristics, which indicates that the nonconcentric rotor will lead to an increase in rotor vibration amplitude, and the appearance of 2X frequency fault characteristics signal. From the spectrum of simulation results, it can be seen that the amplitude of vibration displacement of each measurement point is basically consistent with the test results; meanwhile, the measurement point 3 and measurement point 4 near the connection 2 both show obvious 2X frequency char-

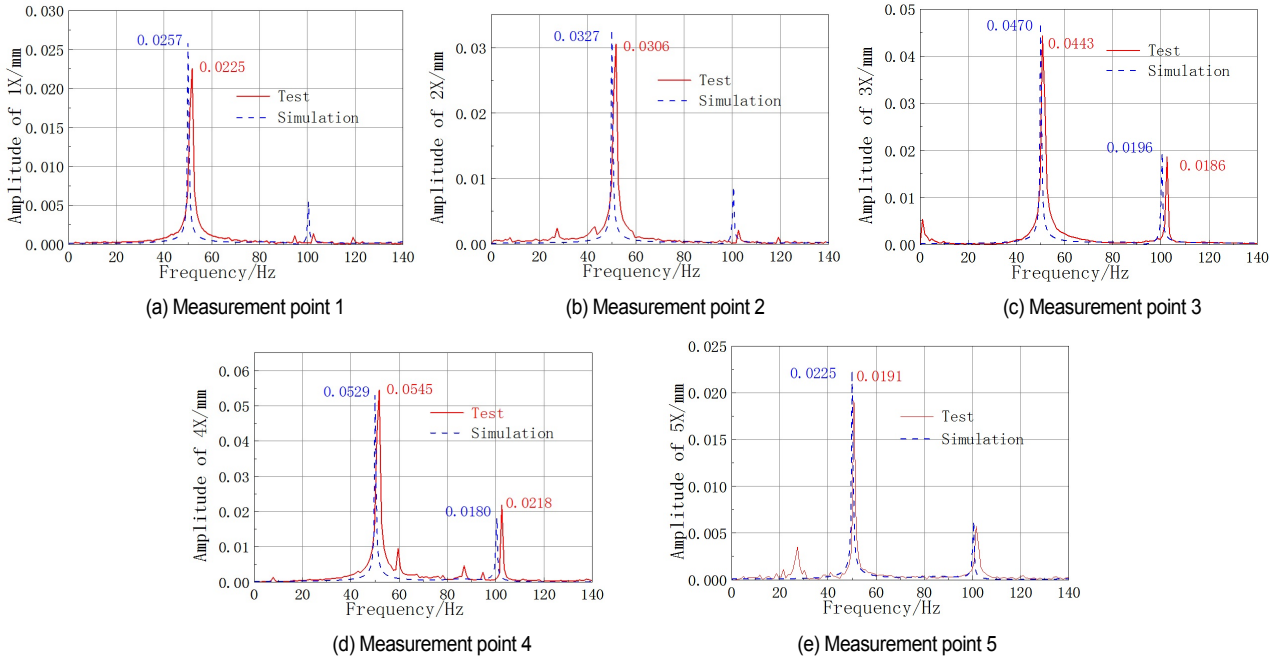

Fig. 24. Spectrum plot of vibration response of measurement point at 0.1 mm endface deviation (3000 r/min).

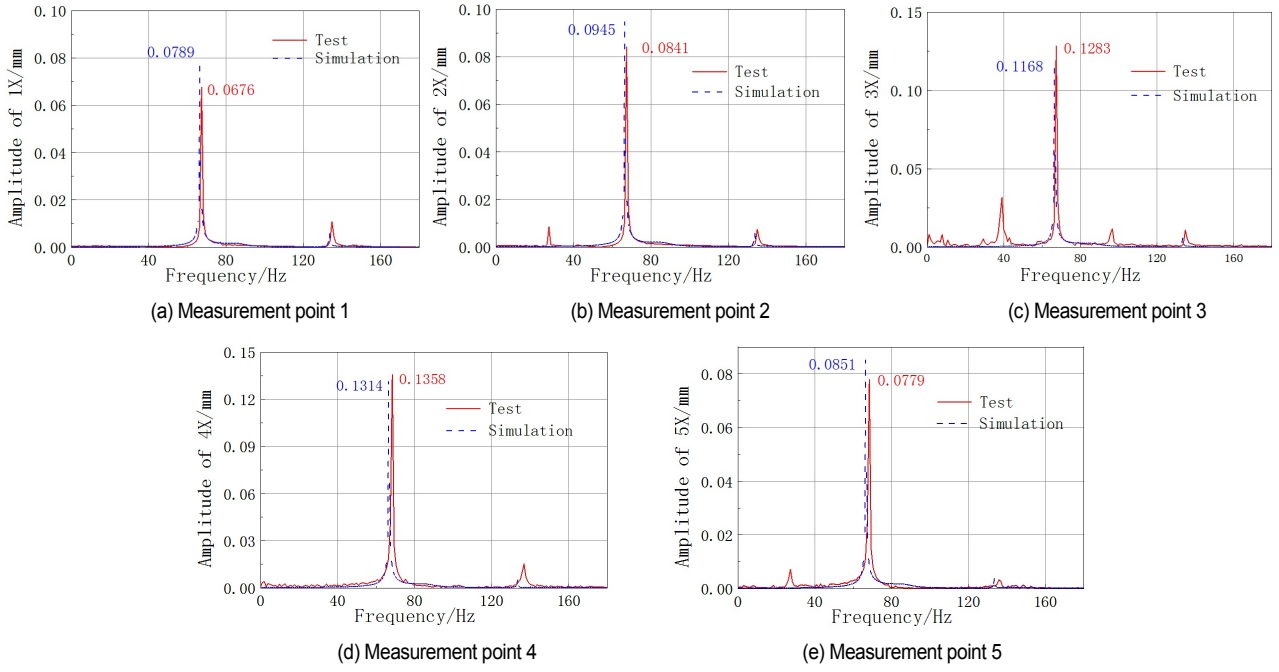

Fig. 25. Spectrum plot of vibration response of measurement point at 0.1 mm endface deviation (4000 r/min).

acteristics, and the 2X frequency amplitude is 0.0196 mm and 0.0180mm respectively, which is also basically consistent with the 2X frequency amplitude of the test results. Therefore, this further verifies the correctness of the nonconcentricity models.

② Speed 4000 r/min

The spectrum plot of the vibration response of each measurement point of the rotor at a speed of 4000 r/min and an endface deviation of 0.01 mm is shown in Fig. 25. From the test results, it can be seen that the vibration response of measurement point 4 is the largest, with a displacement amplitude of 0.1358 mm; the vibration displacement of measurement point 1 is the smallest, with a displacement amplitude of 0.0676 mm; compared with the rotor vibration response at a speed of 4000 r/min under concentric state, the vibration amplitude of each measurement point before and after the rotor increases significantly; taking measurement point 3 as an example, the

Table 3. Comparison of simulation and test results of 1X frequency vibration amplitude at each characteristic speed for 0.1 mm endface deviation.

Speed	Name	Measurement point 1	Measurement point 2	Measurement point 3	Measurement point 4	Measurement point 5
Characteristic speed 3000 r/min	Test amplitude/mm	0.0225	0.0306	0.0443	0.0545	0.0191
	Simulation amplitude/mm	0.0257	0.0327	0.047	0.0529	0.0223
	Error %	14.22 %	6.86 %	6.09 %	2.94 %	16.75 %
Characteristic speed 4000 r/min	Test amplitude/mm	0.0676	0.0841	0.1283	0.1358	0.0779
	Simulation amplitude/mm	0.0789	0.0945	0.1168	0.1314	0.0851
	Error %	16.72 %	12.49 %	8.96 %	3.24 %	9.24 %

Table 4. Comparison of simulation and test results of 2X frequency vibration amplitude at each characteristic speed for 0.1 mm endface deviation.

Speed/r/min	Measurement point 3			Measurement point 4		
	Test amplitude/mm	Simulation amplitude/mm	Error %	Test amplitude/mm	Simulation amplitude/mm	Error %
3000	0.0186	0.0196	5.38	0.0218	0.0180	17.4

vibration displacement amplitude increases from 0.0544 mm to 0.1283 mm. From this, it is obvious that the rotor vibration amplitude will be increased due to the rotor concentricity. The vibration response of each measurement point before and after the rotor is mainly at 1X frequency, and the 2X frequency component is weak and basically negligible. The main reasons include: the first-order critical speed of the rotor tester is about 5200 r/min, and the characteristic speed of 3000 r/min is close to one-half of the first-order critical speed, so it is easy to generate the 2X frequency signal. In addition, the characteristic speed of 4000 r/min is far from one-half of the critical speed, so it is not easy to produce 2X frequency fault characteristic signals. The vibration displacement amplitudes of the rotor simulation results are basically consistent with the experimental results. The vibration response of each measurement point is mainly at 1X frequency and shows smaller 2X frequency characteristics, which is also basically consistent with the experimental results and verifies the correctness of the simulation model.

The simulation and test results of the 1X frequency and 2X frequency vibration amplitudes of each measurement point at different characteristic speeds and 0.1 mm endface deviation are shown in Tables 3 and 4 respectively. At different characteristic speeds, the 1X frequency amplitude of the vibration displacement of each measurement point is similar, and the simulation error does not exceed 20 %. Meanwhile, at 3000 r/min, the 2X frequency vibration amplitudes of measurement point 3 and measurement point 4 are basically the same. This shows that the experimental results achieve good agreement with the simulation results, which verifies the correctness of the dynamic model of rotor nonconcentricity.

5. Conclusions

This paper analyzes the assembly deformation of the simulation tester of the nonconcentric high-pressure rotor, establishes the dynamic model of rotor nonconcentricity, simulates the vibration response of the nonconcentric rotor, and finally verifies the fault characteristics of rotor nonconcentricity through tests. The conclusions are made as below:

1) A contact finite element model of a high-pressure rotor simulation tester with multiple bolted connection surfaces is established, and the assembly deformation state of the rotor when there is endface deviation at the bolted connection interface is simulated and analyzed by extracting the radial displacement of the axis line. The simulation results show that the connection interface 2 with endface deviation is basically fitted, and the rotor deformation is mainly concentrated in the front end of the tapered drum and the connection surface of the turbine rear journal, the rotor axis line as a whole is tapered, and the assembly parameters such as the bolt pretightening force and the number of bolts have little effect on the rotor assembly deformation.

2) Considering the unbalanced excitation force and bending excitation force caused by the rotor nonconcentricity, as well as the additional excitation force of the connection structure, a dynamic model of rotor nonconcentricity is established. Based on the contact finite element model of a high-pressure rotor simulation tester with multiple bolted connection surfaces, the vibration response simulation analysis of nonconcentric rotor is carried out. The calculation results show that the rotor nonconcentricity fault causes an increase in rotor vibration amplitude, and 2X frequency fault characteristics near connection 2 (i.e., near the stop bolt connection structure where endface deviation exists) can be noticed. The vibration response test for rotor nonconcentricity fault at various characteristic speeds is performed using the nonconcentricity simulation tester of the high-pressure rotor simulation tester with multiple bolted connection surfaces. The fault characteristics obtained from the test are similar to the simulation results, thus verifying the correctness of the rotor nonconcentricity fault model.

3) In this paper, only the endface deviation of the connecting 2nd position is considered, and the radial deviation and the stacking effect of the endface deviation and radial deviation of multiple connecting interfaces are not considered. Therefore, in the future work, it is necessary to establish a multi-stage rotor deviation accumulation model based on the actual structure of the high-pressure rotor of the aero-engine, and realize the

assembly control of the rotor with different concentricity through the optimization algorithm, so as to provide technical support for the actual aero-engine assembly process.

Acknowledgments

The authors would like to acknowledge the support of the National Natural Science Foundation of China (Grant No. 52272436) and National Science and Technology Major Project (J2019-IV-004-0071).

References

[1] S. L. Hou, R. Z. Lin, L. Hou and Y. S. Chen, Dynamic characteristics of a dual-rotor system with parallel non-concentricity caused by inter-shaft bearing positioning deviation, *Mechanism and Machine Theory,* 184 (2023) 105262.

[2] Z. Y. Li, W. W. Yuan, S. B. Mao, Y. M. Pu, C. H. Ren and X. Y. Yang, Lightweight intelligent engine vibration prediction model with small samples, *Journal of Engineering Research,* 11 (1) (2023) 100003.

[3] B. Zhang, H. Y. Lu, S. Liu, Y. C. Yang and D. D. Song, Aero-engine rotor assembly process optimization based on Improved Harris Hawk algorithm, *Aerospace*, 10 (1) (2023) 28.

[4] L. Li, Z. Luo, Y. Li, F. He, X. Li and X. Yan, Structural similitude for a scaled rotor system considering stiffness characteristics of bolted joints, *Proceedings of the Institution of Mechanical Engineers, Part C: Journal of Mechanical Engineering Science*, 236 (10) (2022) 5192-5207.

[5] C. Z. Sun, C. T. Li, Y. M. Liu, Z. W. Liu, X. M. Wang and J. B. Tan, Prediction method of concentricity and perpendicularity of aero engine multistage rotors based on PSO-BP neural network, *IEEE Access*, 7 (2019) 132271-132278.

[6] S. L. Hou, L. Hou, S. W. Dun, Y. F. Cai, Y. Yang and Y. S. Chen, Vibration characteristics of a dual-rotor system with non-concentricity, *Machines,* 9 (11) (2021) 251.

[7] C. C. Che, H. W. Wang, R. G. Lin and X. M. Ni, Deep meta-learning and variational autoencoder for coupling fault diagnosis of rolling bearing under variable working conditions, *Proceedings of the Institution of Mechanical Engineers, Part C: Journal of Mechanical Engineering Science*, 236 (17) (2022) 9900-9913.

[8] L. G. Meng, X. D. Li, C. Yue, B. B. Zhao, Y. Ma and Q. C. Sun, Research on tightening process of bolt group in aeroengine rotor, *International Journal of Smart Engineering,* 3 (1) (2019) 35-45.

[9] W. Zhang, Y. S. Ye, D. Chen, Q. K. Han and Y. Ma, Numerical analysis of bolt elastic interaction in non-gasketed flange, *ASME Pressure Vessels and Piping Conference*, Prague, Czech Republic (2) (2018) V002T02A035.

[10] X. Chen, Y. Ma and J. Hong, Vibration suppression of additional unbalance caused by the non-continuous characteristics of a typical aero-engine rotor, *10th International Conference on Rotor Dynamics,* Rio de Janeiro, Brazil, 4 (63) (2018) 34-48.

[11] H. Li, J. F. Huang, Q. Q. Zhang, Y. M. Liu and Y. Jin, The Influence of bolted-flange connection on the coaxial tolerance in accelerator centering assembling, *Journal of Sichuan University (Engineering Science Edition)*, 39 (3) (2007) 155-159.

[12] D. Zhang, Analysis of the influence and control of structural characteristic parameters effect on pivot concentricity for aero-engine, *Aeronautical Science and Technology,* 26 (5) (2015) 22-26.

[13] S. S. Bai, X. Zhai, Y. Y. Ai and W. Ma, The influence of bolted connection on the coaxial tolerance and dynamic analysis in aero-engine casing, *Aeronautical Science and Technology*, 6 (2010) 35-37.

[14] J. C. Nicholas, E. J. Gunter and P. E. Allaire, Effect of residual shaft bow on unbalance response and balancing of a single mass flexible rotor—part II: balancing, *Journal of Engineering for Gas Turbines and Power,* 98 (2) (1976) 182-187.

[15] T. N. Shiau and E. K. Lee, The residual shaft bow effect on dynamic response of a simply supported rotor with disk skew and mass unbalances, *Journal of Vibration and Acoustics,* 111 (2) (1989) 170.

[16] M. Y. Liu, P. Z. Ren, M. F. Liao, M. Zhao and H. Y. Yang, A study on the vibration of flexible rotor due to its initial bending and unbalance, *Journal of Vibration, Measurement and Diagnosis*, 18 (4) (1998) 282-286.

[17] F. S. Lin and G. Meng, Theoretical and experimental analysis on an unbalanced rotor with asymmetric rigidity and initial bending, *Chinese Journal of Applied Mechanics,* 3 (2002) 96-101.

[18] J. Zou, G. M. Dong and J. Chen, Vibration analysis of cracked rotor with initial deflection, *Journal of Vibration and Shock*, 31 (3) (2012) 153-156.

[19] M. H. Yang, G. Chen and P. C. Yu, A method for identifying connection parameters of a static rotor system, *Journal of Vibration and Shock*, 40 (8) (2021) 10-18.

[20] G. Chen, Whole aero-engine vibration coupling dynamics model including modeling of complex ball and roller bearings, *Journal of Aerospace Power*, 32 (9) (2017) 2193-2204.

X. X. Shen is a Ph.D. student in the College of Civil Aviation, Nanjing University of Aeronautics and Astronautics, Nanjing, P. R. China. His research interests include rotor vibration, structural health monitoring, rotordynamics, blade vibration measurement and blade tip clearance measurement.

G. Chen received a Ph.D. degree in the School of Mechanical Engineering from the Southwest Jiaotong University, Chengdu, P. R. China, in 2000. Now he works at the College of Civil Aviation, Nanjing University of Aeronautics and Astronautics, Nanjing, P. R. China. His current research interests include the whole aero-engine vibration, rotor-bearing dynamics, rotating-machine fault diagnosis, pattern recognition and machine learning, signal analysis and processing.